An Unusual Mott Transition in Multiferroic $PbCrO_3$

Shanmin Wang,[1,2,3,§,*,a] Jinlong Zhu,[2,3,4,a] Yi Zhang,[2] Xiaohui Yu,[3,4] Jianzhong Zhang,[3] Wendan Wang,[1] Ligang Bai,[2,6] Jiang Qian,[5] Liang Yin,[7] Neil S. Sullivan,[7] Changqing Jin,[4] Duanwei He,[1,*] Jian Xu,[1] and Yusheng Zhao[2,3,*]

[1] Institute of Atomic & Molecular Physics, Sichuan University, Chengdu 610065, China [2] HiPSEC & Physics Department, University of Nevada, Las Vegas, Nevada 89154, USA [3] Los Alamos National Laboratory, Los Alamos, New Mexico 87545, USA [4] Institute of Physics, Chinese Academy of Sciences, Beijing 100190, China [5] US Synthetic Corporation, 1260 South 1600West, Orem, Utah 84058, USA [6] HPCAT & HPSync, Geophysical Laboratory, Carnegie Institution of Washington, Argonne, Illinois 60439, USA [7] Department of Physics, University of Florida, Gainesville, FL 32611, USA

Submitted to Proceedings of the National Academy of Sciences of the United States of America

Mott insulator in correlated electron systems arises from classical Coulomb repulsion between carriers to provide a powerful force for electron localization. Tuning such an insulator into a metal, the so–called Mott transition, is commonly achieved by 'bandwith' control or 'band filling'. However, both mechanisms deviate from the original concept of Mott, which attributes such transition to the screening of Coulomb potential and associated lattice contraction. Here, we report a pressure–induced isostructural Mott transition in cubic perovskite $PbCrO_3$. At the transition pressure of ~3 GPa, $PbCrO_3$ exhibits significant collapse in both lattice volume and Coulomb potential. Concurrent with the collapse, it transforms from a hybrid multiferroic insulator to a metal. For the first time, these findings validate the scenario conceived by Mott. Close to the Mott criticality at ~300 K, fluctuations of the lattice and charge give rise to elastic anomalies and Laudau critical behaviors resembling the classic liquid–gas transition. The anomalously large lattice volume and Coulomb potential in the low–pressure insulating phase are largely associated with the ferroelectric distortion, which is substantially suppressed at high pressures, leading to the first–order phase transition without symmetry breaking.

Mott transition | multiferroics | PbCrO3 | Mott criticality | isostructural transition

Introduction

Early transition–metal (TM) oxides with partially filled *d* electrons are strongly correlated (*1, 2*). Such correlated systems often present exciting new physics and technologically useful electronic and magnetic properties. Mott transition, characterized by delocalization of *d* electrons, is an attractive phenomenon for exploring correlated nature of electrons (*2, 3*). Since the early failure of the band theory in 1930s, the Coulomb repulsion (U) has been proposed to be a strong force that causes electron localization (*4, 5*). In such electrostatic interaction, the repulsion energy decreases with the compressed lattice because of screening effect (*5-7*). Consequently, as originally predicted by Mott (*5*), the Mott transition is controlled by U at pressures (*P*).

Despite several decades of intensive study, it is still challenging to experimentally validate this view of Mott transition, because U is experimentally difficult to be determined, and for most correlated materials, it is independent of the pressure. For the known Mott systems, they are found to be controlled by either the bandwidth (*e.g.*, organic compound κ–Cl (*8-10*) and Cr–doped V_2O_3 (*11, 12*)) or band filling (*i.e.,* doping of charge carriers into the parent insulator) (*2*). Recently, electronic transitions have frequently been reported in late 3*d* TM oxides (*e.g.,* MnO) (*13-16*), which are theoretically attributed to bandwidth control (*15*) or crystal–field splitting (*17*). For those oxides, a U–controlled mechanism has also been proposed by *Gavriliuk et al.* (*14, 18*); however, the spin crossover, instead of screening effect, is believed to contribute to the decreased U (*14, 18*). Complicating matter further is that the U of $(Mg_{1-x}Fe_x)O$ was computed to increase with pressures (*13*).

TM oxides with a perovskite structure (ABO_3) often exhibit intriguing structural, magnetic, and electronic properties for the study of correlated systems. Among them, $PbCrO_3$ is such a material that can only be synthesized at high pressures. At ambient pressure, it adopts a paramagnetic (PM), cubic structure at room temperature with an anomalously large unit–cell volume and transforms to an antiferromagnetic (AFM) ground state at low temperatures (*19, 20*). The magnetic properties arise from unpaired 3d electrons in Cr (*i.e.,* nominally $3d^2$) with a large U value of 8.28 eV (*19-21*). Under high pressures, an isostructural phase transition (*i.e.,* no symmetry breaking) has recently been reported in $PbCrO_3$ with ~9.8% volume reduction at ~1.6 GPa , it is the largest volume reduction known in transition-metals oxides (*22*). Compared with the low–*P* phase, the high–*P* phase possesses a more 'normal' unit–cell volume (see refs (*22*) and (*21*)) and a moderate U of ~3 eV (*23*), suggesting a collapse of Coulomb repulsion energy at the phase transition. Because of the reduced U, the mobility of 3*d* electrons at high pressures is energetically more favorable, which would lead to the *d*–electron delocalization. Apparently, this is a U–driven Mott transition in $PbCrO_3$ as conceived by Mott. However, to date, the electronic properties of both $PbCrO_3$ phases have only poorly been explored. In particular, controversial electronic states, including semiconductor (*24, 25*), half–metal (*21*), or insulator (*20*), have been reported for the low–P phase. Besides, the crystal structure, elastic and magnetic properties, as well as the underlying mechanism for the isostructural transition are still unsettled issues, calling for rigorous investigation into this material.

With these aims in this work, we present a comprehensive study on $PbCrO_3$ with focus on the *P*–induced electronic

Significance

Understanding of insulator–metal Mott transition in correlated systems has been one of central themes in condensed–matter physics for more than half a century. The original Mott concept of transition mechanism has been proposed in terms of the screening of Coulomb potential at high pressures, which, however, has yet been experimentally validated. Such a scenario, for the first time, is unveiled in multiferroic $PbCrO_3$ with collapse of both the volume and Coulomb potential at high pressures, which is associated with the atomic ferroelectric distortion. In addition, Mott critical behaviors, magnetic and ferroelectric properties, and the isostructural phase transition of this material are also explored. Findings in this work are fundamentally and technologically important for the study of correlated systems.

Reserved for Publication Footnotes

Submission PDF

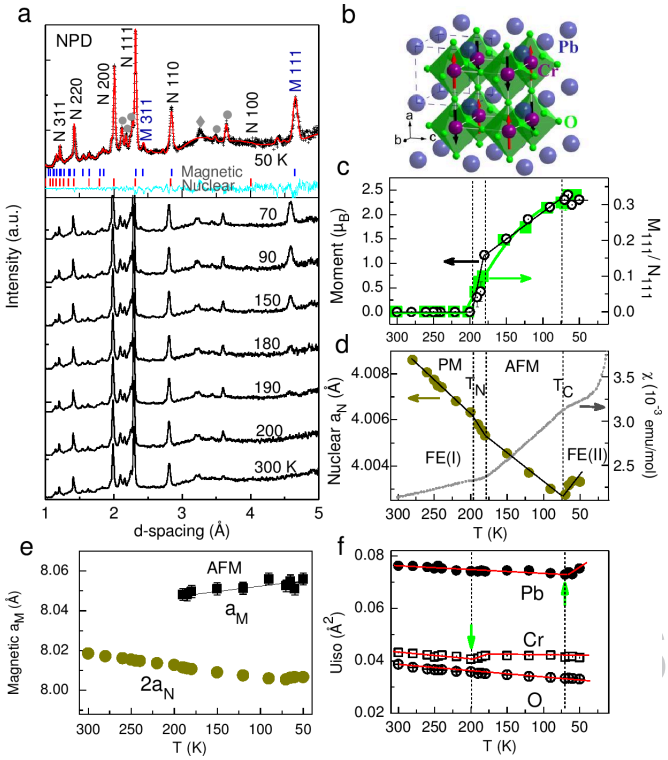

Fig. 1. Low–*T* time–of–flight neutron powder diffraction (NPD) patterns of cubic α–$PbCrO_3$ taken at ambient pressure. **(a)** Selected NPD patterns collected on cooling (bottom) and a refined pattern taken at 50 K (top). Black crosses and red lines represent the observed and calculated profiles, respectively. The difference curves between observed and calculated pattern are shown in cyan. The blue and red tick marks correspond to magnetic and nuclear peak positions. Two impurity phases were observed: Pb_5CrO_8 (·), which is a reaction by–product, and $PbCrO_4$ (•), which was formed during purification. **(b)** Polyhedral view of antiferromagnetic and crystal structures with alternating spin–up and spin–down Cr atoms along *a*–axis. **(c)** Variation with temperature of intensity ratios between magnetic and nuclear peaks, M_{111}/N_{111}, and the refined magnetic moment of Cr. **(d)** Temperature dependent lattice parameter, a_N. Magnetic susptibility data are taken from ref. (*19*). The PM→AFM and ferroelectric FE(I)→FE(II) transitions occur at T_N and T_C, respetively. **(e)** Refined magnetic unit–cell parameter, a_M, as a function of temperature. **(f)**Refined atomic displacement parameter, Uiso, for Pb, Cr, and O.

transition. Our findings unveil a unique Mott transition in this perovskite and a new mechanism underlying the isostructural transition.

Results and Discussion

Fig. 1 shows the low–*T* neutron powder diffraction (NPD) measurement on $PbCrO_3$ at atmospheric pressure. For simplicity, this low–*P* phase is thereafter referred to as α–$PbCrO_3$, and high–P phase is denoted as β phase. In Fig. 1a, α–$PbCrO_3$ can well be refined using a cubic $Pm\bar{3}m$ structure with a lattice parameter of a = 4.0085 (5) Å, which agrees well with reported data (*20, 22, 26*). Compared with XRD patterns, a subset of peaks from nuclear scattering (*e.g.*, the 100 peak) are absent in neutron diffraction patterns. Because neutron scattering lengths (f) satisfy$f_{Pb} = f_{Cr} + f_O$(Fig. S2) (*27*), the α phase should be a pure cubic $PbCrO_3$ rather than a mixture of "$PbCrO_3$ and $CrPbO_3$" as suggested previously (*22, 28*). It has come to our attention that phase transition mechanism of $PbCrO_3$ was reported by *Cheng et al.* (*29*) and *Yu et al.* (*30*) during the submission of this article. However, in their work, either a charge disproportionation mechanism (*i.e.*, $3Cr^{4+} = 2Cr^{3+} + Cr^{6+}$) or a charge transfer process between Pb and Cr were proposed for α–$PbCrO_3$ based on a

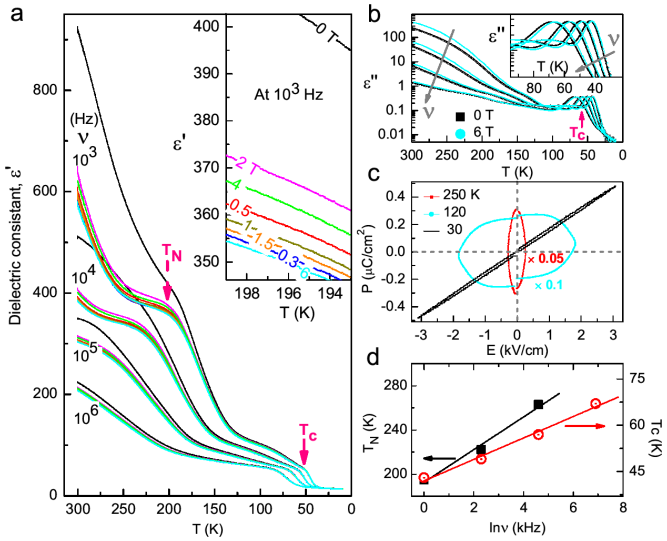

Fig. 2. Dielectric measurement of α–$PbCrO_3$ at ambient pressure. **(a)** Frequency dependent dielectric constant under magnetic fields of B = 0, 2, 4, 0.5, 1, 1.5, 0.3, and 6 T, which were sequentially applied for the measurement. Inset shows an enlarged portion of the data collected at ν = 10^3 Hz. **(b)** Dielectric loss vs. temperature at B = 0 and B = 6 T. An enlarged portion around T_C is inserted to show detail. **(c)** Ferroelectric hysteresis P–E loops measured at selected temperatures of 250, 120, and 30 K. **(d)** T_N and T_c as a function of logarithm of ν (*i.e.*, lnν).

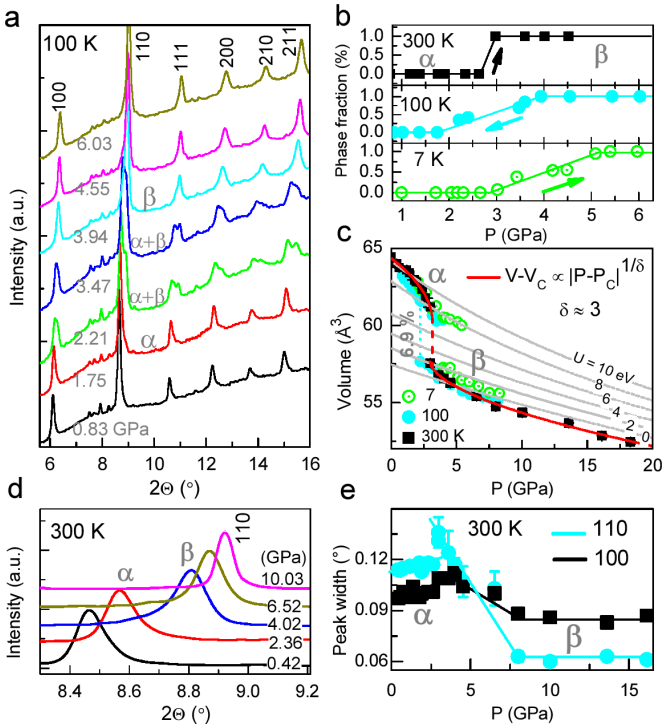

Fig. 3. High–*P* compression of cubic α– and β–$PbCrO_3$ at 7, 100, and 300 K. **(a)** Selected synchrotron XRD patterns at 100 K (λ = 0.424603 Å). **(b)** Phase fraction of β–$PbCrO_3$ as a function of pressure at temperatures of 7, 100, and 300 K. The arrows of → and ← denote compression (300 and 7 K) and decompression (100 K), respectively. **(c)** Obtained volume–pressure data for both phases at 7, 100, and 300 K. The 300 K data are fitted to a power law of $V–V_C \sim |P–P_C|^{1/\delta}$ with δ ≈ 3. Also plotted are first–principles calculations using different U values. **(d)** Enlarged portions of the peak 110 collected at 300 K and pressures up to 10 GPa, **(e)** full width at half maximum of 110 and 100 peaks as a function of pressure.

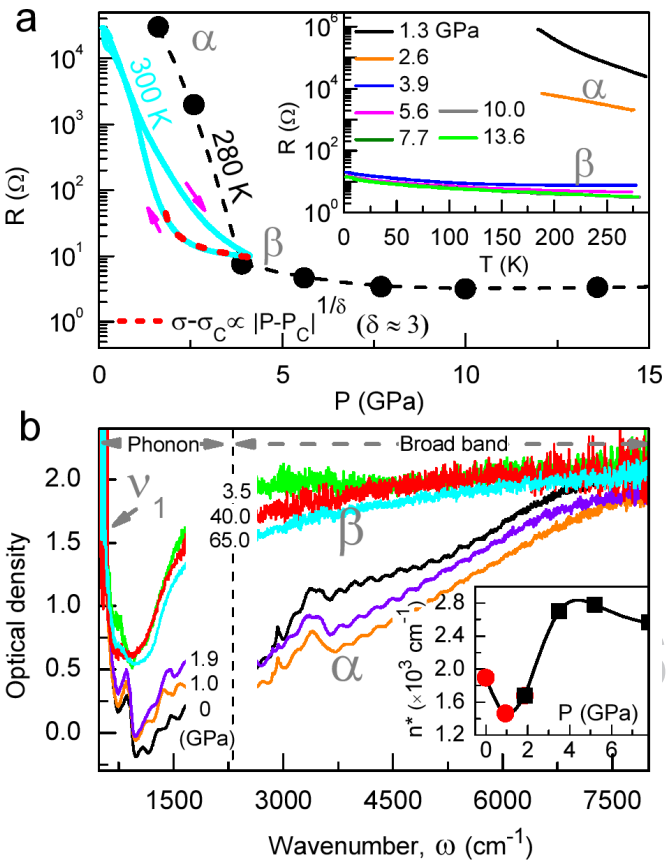

Fig. 4. Pressure dependence of electrical transport behaviors of $PbCrO_3$.(**a**) High–*P* electrical resistance (*R*) measurement in a DAC (inset) at 280 K (blank solid dots) and 300 K (cyan solid lines). The arrows of → and ← denote measurements during compression and decompression, respectively. (**b**) Typical infrared absorption spectra collected at 300 K in a DAC during compression. The data in the frequency range of 1680–2630 cm^{-1}, which corresponds to strong diamond absorption, are removed. An intense peak at ~520 cm^{-1}, v_1, is due to the active stretching mode of CrO_6 octahedrons. Inset shows spectral weight, *n**, as a function of pressure.

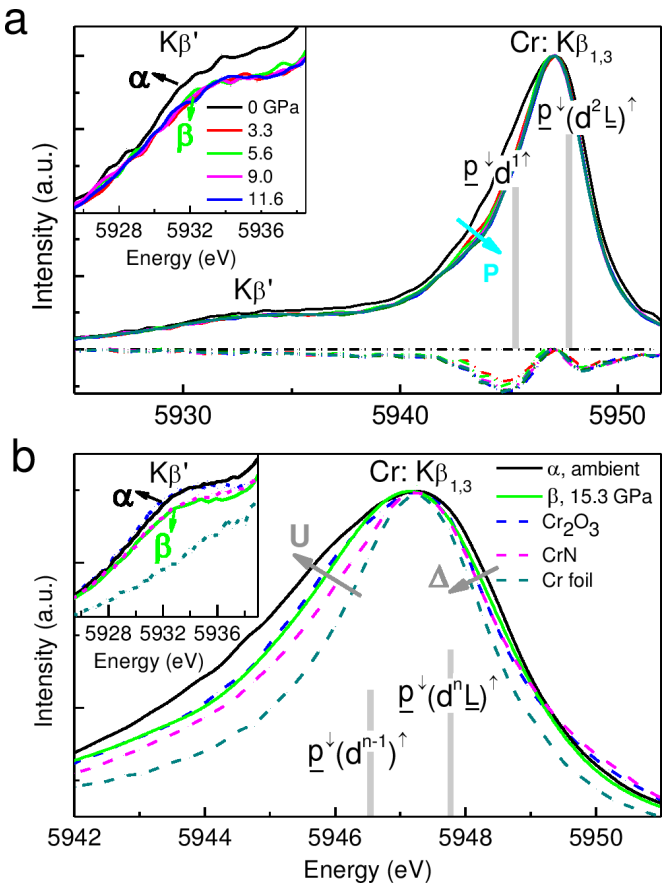

Fig. 5. Cr Kβ XES of $PbCrO_3$. (**a**) High–*P* spectra collected at 300 K. Vertical grey lines denote two split components, and , for the $K\beta_{1,3}$. The lines on the bottom are difference curves between the spectra taken at high pressures and ambient conditions. (**b**) Overlapped spectra for $PbCrO_3$, Cr foil, Cr_2O_3, and CrN. Two components are and , both of which induce an energy shift in U and Δ. For these charge–transfer compounds (*i.e.*, U > Δ, see refs (*44, 45*)), has higher florescence energy. Insets in (a) and (b) are enlarged Kβ'. All spectra are normalized to the peak weight of $K\beta_{1,3}$, and the spectrum energies in (b) are also normalized to that of $PbCrO_3$ (see original data in Fig. S10).

distorted cubic structure (*29*) or a low–symmetry orthorhombic structure (*30*). Such proposed structures would lead to the presence of 100 peak in neutron diffraction patterns, which is contrary to our experimental observations (Fig. 1a and Fig. S2).

A paramagnetic (PM)–antiferromagnetic (AFM) transition is observed at $T_N \approx 190$ K, and the intensity of a magnetic peak 111 (M 111) increases gradually on cooling (Fig. 1a). The magnetic structure has been refined using a G–type AFM model as adopted previously (*20, 31*), as shown in Fig. 1b. Below 90 K, the refined magnetic moment of Cr reaches a plateau value of 2.2(1) μ_B (Fig. 1c), close to previously reported (*20*). A similar trend is also found in the peak intensity of M 111 (also see Fig. S3). In Fig. 1d, the variation with temperature of lattice parameters indicates an abnormal contraction at T_N due to spontaneous magnetostriction and an unexpected expansion at $T_C \approx 65$ K associated with a ferroelectric transition as discussed below. Concurrently, anomalous magnetic susceptibility (χ) has been observed in Fig. 1d (see ref. (*19*)) at temperatures near T_N. Interestingly, the magnetic ordering is incommensurate with that of the crystal lattice (*i.e.,* $a_M > 2a$) (Fig. 1e), suggesting a 'frustrated' magnet. As pointed out by Cheong *et al.* (*32*), this magnetic frustration drives spatial variations of magnetization and eventually results in ferroelectricity. Besides the refined atomic displacement parameters, Uiso, show two possible ferroelectric transitions at T_N and T_C (Fig. 1f) associated with Cr and Pb atoms, respectively.

To investigate ferroelectric properties, dielectric measurement has been performed on α–$PbCrO_3$ (Fig. 2). The measured dielectric constant, ε', is significantly reduced when the temperature is decreased because dielectric oscillators are thermally activated or when the frequency is increased (Fig. 2a) because of the space–charge polarization, which partially contributes to ε', is progressively suppressed at higher frequencies (*33*). Above T_N, ε' is sensitive to the external magnetic field (B) at all selected frequencies, suggesting a strong magnetoelectric effect. At frequencies of 10^3 and 10^4 Hz, there is an asymptotic leveling–off in ε' at all applied magnetic field. The coupling between magnetism and ferroelectricity at T_N indicates that α–$PbCrO_3$ is an 'improper' ferroelectric (ref. (*32*)).

Upon further cooling, there is a step–like reduction in ε' at T_C due to a ferroelectric transition associated with Pb atoms. For Pb– or Bi–bearing perovskite, the lone–pair $6s^2$ electrons in such ions often deviate from the centrosymmetry in oxygen surroundings, leading to 'proper' ferroelectrics, such as $BiFeO_3$ and $Pb(Fe_xW_{1-x})O_3$ (*32*). Obviously, α–$PbCrO_3$ exhibits a 'proper' ferroelectric transition at T_C (Fig. 2a), which is correlated with the observed lattice anomalies (see Figs 1d and 1f). This ferroelectric transition also shows a peak in the dielectric loss measurement around T_C (Fig. 2b), which is independent of the

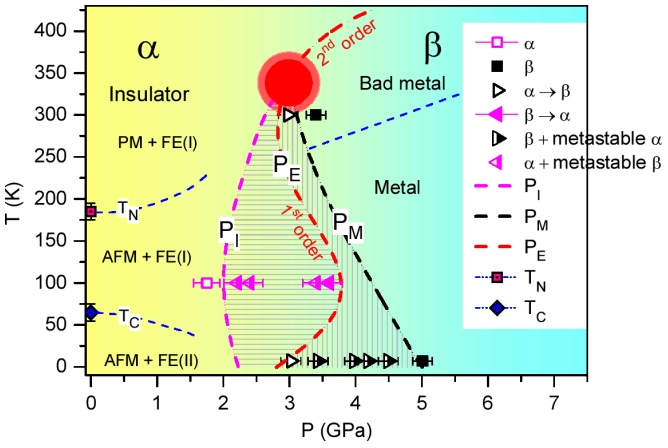

Fig. 6. Pressure–temperature phase diagram for Mott transition between α– and β–$PbCrO_3$. The first–order equilibrium phase boundary (red dashed curve) is bracketed by the onsets of α→β and β→α transitions. It presumably ends at a critical point (red solid circle) because the P–V data at 300 K already show signs of continuous variation across the α–β transition (Fig. 3c). Beyond the solid–solid critical point, the structural transition is second order. Two spinodal lines, P_I (dashed magenta, defining the lower bound for metastable β phase) and P_M (dashed black, defining the upper bound for metastable α phase), delimit a two–phase coexisting region. The area hatched by horizontal lines for α + metastable β and the one hatched by vertical lines for β + metastable α. All blue dash lines, which are highly schematic and not constrained in this work, delineate possible boundaries of the magnetic, ferroelectric, and bad metal–to–Fermi–liquid metal transitions discussed in text. Two different ferroelectric phases are defined as FE(I) and FE(II) with a transition temperature of T_C.

external magnetic field, because the polarization of Pb atoms correlates only weakly with the magnetic spin of Cr. Thus, we conclude that α–$PbCrO_3$ is a hybrid multiferroic system with both 'proper' and 'improper' ferroelectric characters. Fig. 2c shows the polarization–electric (P–E) field hysteresis loops at selected temperatures. Above 120 K, the polarization cannot be determined because of the current leakage. At 30 K, a narrow ferroelectric–like P–E loop was observed (Fig. 2c). In addition, the obtained T_N and T_C increase exponentially with the frequency (Fig. 2d). Also noted is that the $Pm\bar{3}m$ symmetry is structurally unfavorable for a 'normal' ferroelectric, because the electric polarization would induce structural distortion. From this viewpoint, cubic α–$PbCrO_3$ may be an exception with unusual ferroelectric properties, which warrants further experimental and theoretical work aiming at the ferroelectricity of this compound based on single–crystal sample. However, as proposed in refs (*29, 30*), no ferroelectric effect was taken into account in the charge disproportionation or transition models for α–$PbCrO_3$.

The high–*P* structural stability of α–$PbCrO_3$ was studied by XRD at three different temperatures of 7, 100, and 300 K, respectively. Fig. 3a shows selected patterns taken at 100 K during decompression (the data collected at 300 and 7 K during compression are shown in Fig. S5). The high–P β phase adopts the same cubic structure as the α–$PbCrO_3$ (Fig. S6), confirming the previously reported isostructural transition (*22*). No further structural transition was observed at pressures up to ~20 GPa or temperatures down to 4.5 K (Fig. S4). At 300 K, the α→β transition starts at ~2.9 GPa and is complete at ~3.1 GPa, indicating that α–$PbCrO_3$ can metastably coexist with β–$PbCrO_3$ in a narrow pressure range (*i.e.*, $\Delta P \approx 0.2$ GPa). As expected from the kinetics of phase transformation, the metastable region for α–$PbCrO_3$ increases with decreasing temperatures, extended to $\Delta P > 2$ GPa at 7 K (Fig. 3b). Apparently, the coexisting phase regime is constrained by two spinodal curves that end at a critical point near ~300 K and ~3 GPa in the P–T phase diagram, which resembles those observed in the known Mott–transition systems, including κ–Cl(*8-10*) and Cr–doped V_2O_3(*11, 12*).

Fig. 3c summarizes the derived volume (V)–P data. At 100 K, there is a ~6.9% volume reduction at the phase transition. Obviously, α–$PbCrO_3$ is elastically more compressible than the β phase. At 300 K, the crystal lattice in the α–$PbCrO_3$ is promptly softened in the vicinity of the phase transition. Similar elastic anomalies have also been found in other crystalline solids when the critical point is approached (*34*), such as κ–Cl and Cr–doped V_2O_3 (*35-37*), which can be evaluated using the critical scaling theory (*37, 38*). For $PbCrO_3$, the lattice degree of freedom can be well described by a power law, $V–V_C \propto |P–P_C|^{1/\delta}$, with an exponent of $\delta \approx 3$ at 300 K, where V_C and P_C are the critical volume and pressure, respectively, at the critical point. The same exponent can also be obtained from the density–pressure relationship. This behavior is analogous to the classical liquid–gas critical point (*38*), which has been reported for the Mott transition in Cr–doped V_2O_3 (*11*). All these evidences suggest that the α→β transition in $PbCrO_3$ is an isostructural Mott transition with a critical point at ~300 K and 3 GPa. Furthermore, this Mott criticality exerts an internal pressure on the elastic system to which the crystal lattice responds (*37*). Consequently, the elastic modulus vanishes at the critical point due to the breakdown of Hooke's law, a signature of crossover from Ising criticality to Landau critical behavior with a mean–field exponent of $\delta = 3$ (see ref. (*37*)). Under subcritical conditions (*e.g.*, at 7 and 100 K), the P–V relations show abrupt reduction in the volume at the transition pressure (Fig. 3c), indicating that the phase transition is the first order.

To better understand this fascinating phase transition, *ab initio* calculations have been performed on $PbCrO_3$ using a GGA + U method. Such–computed P–V data are plotted in Fig. 3c. For both phases, the corresponding U values are sensitive to pressures. At ambient conditions, the calculated volume of α–$PbCrO_3$ corresponds to a U of ~10 eV, which decreases gradually to ~7 eV at the transition pressure. Similarly, the calculated U for β–$PbCrO_3$ varies from ~3 to 0 eV as the pressure increases from ~3 to 8 GPa, indicating a substantial reduction of U at the phase transition. However, previous simulations were performed at a certain fixed value of U, which would introduce significant errors in the bulk modulus calculations (Fig. S7) (*22, 23*). In fact, for such a Mott system, further calculations using dynamical mean–field theory (DMFT) would be more suitable for exploring the detail of Mott transition in $PbCrO_3$ as this theoretical scheme has successfully been exerted for other Mott systems (*17, 39*).

Because of the ferroelectric displacement, the XRD peaks of α–$PbCrO_3$ are largely broadened (see Figs 3d–e). As the pressure increases, they gradually sharpen and plateau at a relatively small linewidth for metallic β–$PbCrO_3$ (Fig. 3e) when the ferroelectric distortion is no longer involved.

The *P*–induced metallization of α–$PbCrO_3$ is identified using the high–*P*/low–*T* electrical resistance (R) measurement (Fig. 4a). At ambient conditions, the α–$PbCrO_3$ is an insulator and has a large negative temperature coefficient of resistance (TCR) (inset in Fig. 4a). The β–$PbCrO_3$ falls into the regime of metal although it has a small negative TCR, which may arise from the grain boundaries effect. The metallic nature of β–$PbCrO_3$ has also recently been reported (*24, 29*), which supports our conclusion. As expected for a critical behavior, the measured resistance decreases continuously as the pressure crosses the α→β transition at 300 K. This behavior indicates that the electronic transition from an insulator to a 'bad' metal is the second order (*9*) although the structural transition is the first order. Interestingly, the conductivity (σ) at 300 K obeys a power law of $\sigma–\sigma_c \propto |P–P_C|^{1/\delta}$ with $\delta \approx 3$ (Fig. S8). Thus, both the conductance and crystal lattice of $PbCrO_3$ exhibit the same Landau mean–field behaviors (Fig. 3c), indicating that there is a strong coupling

Submission PDF

between electronic and elastic degrees of freedoms around the Mott end point.

The insulator–metal transition can further be determined using the optical method and understood in terms of the polaron theory (*40, 41*). Coupled with the metallization process, the transition of polarons from localized states into the continuum gives rise to a broad band located in near infrared (IR) region (*40*). Therefore, the delocalization of polarons can be probed by the IR spectroscopy. The measured frequencies in Fig. 4b can empirically be divided into two sub–regions: the phonon and the broad–band. The latter absorption is attributed to the photoionization of polarons and is highly sensitive to the degree of the polaron localization. The pressure–dependent spectral weight (inset of Fig. 4b), n^*, which is a frequency–integrated absorbance at 3800–6400 cm^{-1}, provides a measure of polaron mobility (*40, 41*). Upon initial compression, the broad–band optical density, $O_d(\omega)$, and n^* decrease with increasing pressures. Near 1 GPa, the trend is reversed and the absorption starts to increase. The unexpected decrease in absorption is due to the increased binding energy of polarons, suggesting an enhanced insulating state in α–$PbCrO_3$. Above 1.0 GPa, both $O_d(\omega)$ and n^* increase drastically before they reach asymptotic levels near 3.5 GPa, implying that polarons are delocalized at high pressures. In the phonon region, an intense peak located at ~520 cm^{-1} corresponds to the active stretching mode (Fig. S9).

The Cr *K*β x–ray emission spectroscopy (XES) was performed under high pressures on $PbCrO_3$. All spectra in Fig. 5a show a main fluorescence peak ($K\beta_{1,3}$) at 5947 eV and a satellite peak (Kβ') near 5933 eV, the latter of which arises from the decay of Cr 3*p* electrons to the 1s core holes created during *K*–shell absorption (*42, 43*). Such–formed Cr 3*p* core holes ($\underline{p}$) have net spin–up (↑) or spin–down (↓) moments to magnetically interact with the outer and unpaired 3*d* electrons (*i.e.*, 3*p*3*d* exchange interaction), which would give rise to the final states of ($^3\underline{p}^{\downarrow 3}d^{\uparrow}$) and ($^3\underline{p}^{\uparrow 3}d^{\uparrow}$) responsible for $K\beta_{1,3}$ and Kβ', respectively. Above the pressure of Mott transition, the intensity of Kβ' is apparently lowered (Fig. 5a) to an asymptotic level, indicating a magnetic collapse due to the partial delocalization of 3*d* electrons in β–$PbCrO_3$.

The spectral profile of XES can be analyzed using the metal–ligand cluster model (*43, 44*). Because of charge transfer, the d^n ground state is split into multiple configurations in the process of photoemission (*2, 45*), including d^{n-1} and $d^n\underline{L}$ (where $\underline{L}$ denotes a ligand hole in the 2*p* orbital), although traditional ones of d^n and $d^{n+1}\underline{L}$ have also been reported (*46*). For Cr in $PbCrO_3$, the split configurations are d^1 and $d^2\underline{L}$; the $K\beta_{1,3}$ is thus split into two components of $\underline{p}^{\downarrow}(d^1)^{\uparrow}$ and $\underline{p}^{\downarrow}(d^2\underline{L})^{\uparrow}$ with energy shifts in U and Δ, respectively (where Δ is the charge transfer energy from ligand to metal) (*7*). Above the pressure of phase transition, the $K\beta_{1,3}$ peak of $PbCrO_3$ is abruptly sharpened on the low–energy side (Fig. 5a), suggesting a reduction in U. Compared with the simplest case of Cr foil, the $K\beta_{1,3}$ peaks in both α– and β–$PbCrO_3$ are substantially broadened on the low–energy side, which further confirms that the linewidth of $K\beta_{1,3}$ is U–dependent. The broadening on the high–energy side is less severe than that of low–energy side, suggesting that in $PbCrO_3$ U is greater than Δ (*i.e.*, a charge–transfer type band structure). From the intensity of Kβ', we infer that the local magnetic moments of α– and β–$PbCrO_3$ may be comparable to those of Cr_2O_3 and CrN, respectively, both of which also exhibit charge–transfer–type band structure (*47, 48*).

A tentative phase diagram of $PbCrO_3$ is shown in Fig. 6. The first–order equilibrium phase boundary for the insulator–metal transition was bracketed by the onsets of α → β transition during compression and those of β → α transition during decompression. It presumably ends at a critical point around 3 GPa and 320 K, beyond which the structural transition is the second order. Such constructed P–T phase diagram resembles the conventional liquid–gas transition (ref. (*38*)) with α– and β–$PbCrO_3$ correspond to the 'gas' and 'liquid' states under subcritical conditions. On each side of the first–order phase boundary there is a spinodal curve that defines a two–phase coexisting region, the left region for α + metastable β (hatched by horizontal lines) and right region for β + metastable α (hatched by vertical lines). Such a unique spinodal boundary is associated with complicated Mott transition processes that involve magnetic, structural, electronic, and ferroelectric transitions. The similar spinodal lines have previously been reported for κ–Cl (*8-10*) and Cr–doped V_2O_3 (*11*), the two known Mott systems. For α–$PbCrO_3$, the PM–AFM transition temperatures, T_N, are expected to increase with pressures due to enhanced magnetic exchange under high pressures, which has also been predicted in this material system (*49*). Approaching the Mott transition pressure, the T_C would decrease rapidly to zero with vanishing ferroelectricity because of metallization. For β–$PbCrO_3$ characterized as a 'bad' metal at 280 and 300 K (Fig. 4a), it is expected that a Fermi–liquid metal prevails at lower temperatures as reported in other Mott systems (*8, 9, 11*).

Spin–orbit coupling and collinear spins below T_N in α–$PbCrO_3$ should split and re–order the two t_{2g} orbitals in Cr: one $d_{||}$ orbital (*xy*) and one π^* orbital (*yz* or *zx*) (*3, 49*), which would give rise to a cooperative distortion of cubic crystal to a lower–symmetry tetragonal structure (*3, 23*). However, no symmetry breaking is observed. On the other hand, the ferroelectrically induced displacement in Cr atoms leads to distortion of CrO_6 octahedra and ligand–field splitting, which removes the degeneracy of the outer t_{2g} orbital and gives rise to a local potential well, which would in turn localize the t_{2g} electrons. Such a scenario of electron localization is similar to that of Jahn–Teller distortion (*3*). At high pressures, the suppression of ferroelectric distortion causes a volume collapse and profoundly screened U, and consequently, increased probability of doubly occupied sites (*i.e.,* the mobility of electrons), which eventually leads to a Mott transition.

Submission PDF

Experimental Section

Commercially available high–purity PbO (>99.9%, 10 um) and CrO_2 (>99.5%) powders in a molar ratio of PbO : CrO_2 = 1.05 : 1 were homogeneously mixed for the synthesis of $PbCrO_3$ through a solid state reaction at 8 GPa and 1373 – 1473 K for 30 min, given by

$PbO + CrO_2 = PbCrO_3$ (1).

The excess PbO was used to eliminate CrO_2 impurity. High P–T synthesis was carried out in a cubic press at US Synthetic Corp. and a Kawai–type multi–anvil apparatus installed at Sichuan University. Before experiment, the mixed sample powders were compacted into a cylindrical pellet of 13 mm in height and 13 mm in diameter. A Mo capsule was used to isolate the sample from a graphite heater to avoid possible contamination. In each experimental run, the sample was first compressed to a desired pressure, and then heated to a target temperature and soaked for 30 min before quench to room temperature and subsequent decompression to ambient conditions. More experimental detail can be found elsewhere (*50, 51*). The recovered run product was ground into powders and washed in acetic or diluted nitric acid to remove excess PbO, followed by drying in an oven at 333 K. For the electrical resistivity and dielectric measurements, high–density bulk samples were prepared by sintering purified powders at 8 GPa and 1373 K for 1 hour.

The final run products were characterized by x–ray diffraction (XRD) with Cu Kα radiation and a field emission scanning electron microscope (SEM). Low–T time–of–flight neutron diffraction measurement was performed at the HiPPO flightpath of Los Alamos Neutron Science Center (LANSCE), Los Alamos National Laboratory. The crystal and magnetic structures were determined from Rietveld refinement of the x–ray and neutron diffraction data using the GSAS software.

Dielectric measurements were conducted at selected electric–field frequencies of $\nu = 10^3$, 10^4, 10^5, and 10^6 Hz on a cuboid bulk sample with mirror and parallel surfaces (surface area S = 0.159 cm^2 and thickness d = 0.162 cm). At each frequency, the low–T capacitance (C) was measured at different external magnetic fields of B = 2, 4, 0.5, 1, 1.5, 0.3, and 6 Tesla to investigate their effects on ferroelectricity. The dielectric constant, ε, was calculated from *C*, *S*, and *d* (*i.e.*, $C = \varepsilon \cdot S/d$ for a parallel plate capacitor). The polarization–electric–field (*P*–*E*) hysteresis loop was measured at 250, 120, and 30 K, respectively, at external voltages of 50, 300, and 500 V.

High–*P* angle–dispersive synchrotron XRD and x–ray emissions spectroscopy (XES), infrared (IR) absorption spectroscopy, and electrical resistance

experiments were performed in diamond anvil cells (DACs) at the HPCAT 16BM–D and 16IDD beamlines of APS, the U2A beamline of NSLS–I, and the Institute of Physics, CAS, China, respectively. In each experiment, a sample chip of 70 × 70 ∼ 90 × 90 μm^2 was loaded into the sample hole in a gasket pre–indented to ∼25–40 micron and a few ruby balls were loaded to serve as the internal pressure standard. For these experiments, the corresponding gaskets were stainless steel, beryllium, rhenium, and cBN mixed with epoxy. Neon gas and NaCl were used as pressure–transmitting media in synchrotron XRD and resistance experiments, respectively, and the silicon oil was used in the XES and IR absorption experiments. High–P XRD data were taken from two separate experimental runs, one conducted at room temperature (run #1, 300 K) and the other at low temperatures (run #2, including 7 and 100 K). Before low–T XRD experiment, the DAC was installed in a liquid–flow helium cryostat and the cell pressure was remotely controlled through a gas loading system. The temperature and pressure were measured using thermocouple and on–line ruby system, respectively. At target low temperature of 7 K, the XRD data were taken during compression up to 8 GPa, followed by warming the sample to 100 K and the XRD data were taken during decompression. The XES and IR absorption measurements were performed at room temperature. The high–P/low–T electrical resistance measurement was carried out in a PPMS system; more experimental details can be found elsewhere (*52*).

First–principles calculations were performed for $PbCrO_3$ using the density functional theory (DFT) and generalized gradient approximation (GGA) + U approach. The projector augmented–wave (PAW) and pseudopotential were implemented in VASP and used in the calculations with a plane–wave basis–set, which was truncated at the cutoff energy of 500 eV to obtain a 2 meV convergence in the total energy per atom (*53*). Before calculations, the unit cell and atomic coordination were fully relaxed. The crystal symmetry was removed by imposing different magnetic moments on Cr ions and the calculations were spin–polarized.

Acknowledgments.

This work is partially supported by HiPSEC, which is a DOE NNSA Center of Excellence operated under Cooperative Agreement DE–FC52–06NA27684, and UNLV start–up funding to Y. Zhao. This work was also supported by the China 973 Program (Grant No. 2011CB808205), and the NNSF of China (Grant Nos. 11427810 & 51472171). Portions of this work were performed at HPCAT at APS, which is supported by DOE–NNSA under Award No. DE–NA0001974, DOE–BES under Award No. DE–FG02–99ER45775, and DOE–BES under Contract No. DE–AC02–06CH11357. This research is partially supported by Los Alamos National Laboratory, which is operated by Los Alamos National Security LLC under DOE Contract DE–AC52–06NA25396. A portion of this work was performed at the NHMFL, which is supported by NSF (No. DMR-1157490), the State of Florida, and the U.S. DOE. We thank A. Serafin, and J.–S. Xia for ferroelectric properties measurement at the NHMFL and thank C. Park, C. Kenney–Benson, H. Yan, Y. Xiao, Z. Liu, and S. Tkachev for help on high–P XRD, emission, and infrared absorption measurements and gas loading for diamond–anvil cells. We also thank Prof. C. Chen, A. Alvarado, and J. Attapattu for help on theoretical calculations. **Author information** This article is a PNAS Direct Submission. §Present address: Chemical & Engineering Materials Division, Oak Ridge National Laboratory, Oak Ridge, TN 37831, USA. [a]S.Wang and J.-L. Zhu contributed equally to this work. *To whom correspondence may be addressed: ShanminWang@gmail.com (S. W.), DuanweiHe@scu.edu.cn (D. H.), or Yusheng.Zhao@unlv.edu (Y. Z.) *Notes* The authors declare that they have no competing financial interests.

Submission PDF

1. Goodenough JB (1971) Metallic oxides. *Prog Solid State Chem* 5(0):145-399.
2. Imada M, Fujimori A, & Tokura Y (1998) Metal-insulator transitions. *Rev Mod Phys* 70(4):1039-1263.
3. Goodenough JB & Zhou JS (1998) Localized to Itinerant Electronic Transitions in Transition-Metal Oxides with the Perovskite Structure. *Chem Mater* 10(10):2980-2993.
4. Mott N (1984) Metals, nonmetals and metal-nonmetal transitions: some recollections. *Rep Prog Phys* 47(8):909.
5. Mott NF (1968) Metal-Insulator Transition. *Rev Mod Phys* 40(4):677-683.
6. Mott NF (1949) The Basis of the Electron Theory of Metals, with Special Reference to the Transition Metals. *Proc Phys Soc London, Sect A* 62(7):416.
7. Goodenough JB (1967) Characterization of d electrons in solids by structure I. Localized vs collective electrons. *Mater Res Bull* 2(1):37-48.
8. Kagawa F, Miyagawa K, & Kanoda K (2009) Magnetic Mott criticality in a κ-type organic salt probed by NMR. *Nat Phys* 5(12):880-884.
9. Jerome D (2009) Metal-insulator transitions: The problem with spins. *Nat Phys* 5(12):864-865.
10. Limelette P, *et al.* (2003) Mott transition and transport crossovers in the organic compound κ-(BEDT-TTF)$_2$Cu[N(CN)$_2$]Cl. *Phys Rev Lett* 91(1):016401.
11. Limelette P, *et al.* (2003) Universality and Critical Behavior at the Mott Transition. *Science* 302(5642):89-92.
12. McWhan DB, Rice TM, & Remeika JP (1969) Mott transition in Cr-doped V_2O_3. *Phys Rev Lett* 23(24):1384-1387.
13. Tsuchiya T, Wentzcovitch RM, da Silva CRS, & de Gironcoli S (2006) Spin transition in magnesiowüstite in Earth's lower mantle. *Phys Rev Lett* 96(19):198501.
14. Gavriliuk AG, *et al.* (2008) Another mechanism for the insulator-metal transition observed in Mott insulators. *Phys Rev B* 77(15):155112.
15. Cohen RE, Mazin II, & Isaak DG (1997) Magnetic collapse in transition metal oxides at high pressure: Implications for the Earth. *Science* 275(5300):654-657.
16. Gavriliuk AG, Trojan IA, & Struzhkin VV (2012) Insulator-metal transition in highly compressed NiO. *Phys Rev Lett* 109(8):086402.
17. Kunes J, Lukoyanov AV, Anisimov VI, Scalettar RT, & Pickett WE (2008) Collapse of magnetic moment drives the Mott transition in MnO. *Nature Mater* 7(3):198-202.
18. Lyubutin IS, Ovchinnikov SG, Gavriliuk AG, & Struzhkin VV (2009) Spin-crossover-induced Mott transition and the other scenarios of metallization in 3d^n metal compounds. *Phys Rev B* 79(8):085125.
19. Arévalo-López ÁM, Dos santos-García AJ, & Alario-Franco MA (2009) Antiferromagnetism and Spin Reorientation in "PbCrO3". *Inorg Chem* 48(12):5434-5438.
20. Komarek AC, *et al.* (2011) Magnetic order, transport and infrared optical properties in the ACrO$_3$ system (A = Ca, Sr, and Pb). *Phys Rev B* 84(12):125114.
21. Lu Y, He D, Peng F, & Cheng X (2013) The mystery of abnormally large volume of $PbCrO_3$ with a structurally consistent Hubbard U from first-principles. *Eur Phys J B* 86(8):1-5.
22. Xiao W, Tan D, Xiong X, Liu J, & Xu J (2010) Large volume collapse observed in the phase transition in cubic $PbCrO_3$ perovskite. *Proc Nat Acad Sci USA* 107(32):14026-14029.
23. Ganesh P & Cohen RE (2011) Orbital ordering, ferroelasticity, and the large pressure-induced volume collapse in $PbCrO_3$. *Phys Rev B* 83(17):172102.
24. Wu M, *et al.* (2014) Pressure-Induced Valence Change and Semiconductor–Metal Transition in $PbCrO_3$. *J Phys Chem C* 118(40):23274-23278.
25. Wang W-D, He D-W, Xiao W-S, Wang S-M, & Xu J-A (2013) Electrical characterization in the phase transition between cubic $PbCrO_3$ perovskites at high pressures. *Chin Phys Lett* 30(11):117201.
26. Chamberland BL & Moeller CW (1972) A study on the $PbCrO_3$ perovskite. *J Solid State Chem* 5(1):39-41.
27. Sears VF (1992) Neutron scattering lengths and cross sections. *Neutron News* 3(3):26-37.
28. Wang B-T, Yin W, Li W-D, & Wang F (2012) First-principles study of pressure-induced phase transition and electronic property of $PbCrO_3$. *J Appl Phys* 111(1).
29. Cheng J, *et al.* (2015) Charge disproportionation and the pressure-induced insulator–metal transition in cubic perovskite $PbCrO_3$. *Proc Nat Acad Sci USA* 112(6):1670-1674.
30. Yu R, *et al.* (2015) Melting of Pb Charge Glass and Simultaneous Pb–Cr Charge Transfer in PbCrO3 as the Origin of Volume Collapse. *J Am Chem Soc* 137(39):12719-12728.
31. Roth WL & DeVries RC (1967) Crystal and magnetic structure of $PbCrO_3$. *J Appl Phys* 38(3):951-952.
32. Cheong S-W & Mostovoy M (2007) Multiferroics: a magnetic twist for ferroelectricity. *Nature Mater* 6(1):13-20.
33. Rao KV & Smakula A (1965) Dielectric properties of cobalt oxide, nickel oxide, and their mixed crystals. *J Appl Phys* 36(6):2031-2038.
34. Greaves GN, Greer AL, Lakes RS, & Rouxel T (2011) Poisson's ratio and modern materials. *Nature Mater* 10(11):823-837.
35. de Souza M, *et al.* (2007) Anomalous lattice response at the Mott transition in a quasi-2D organic conductor. *Phys Rev Lett* 99(3):037003.
36. Populoh S, Wzietek P, Gohier R, & Metcalf P (2011) Lattice softening effects at the Mott critical point of Cr-doped V_2O_3. *Phys Rev B* 84(7):075158.
37. Zacharias M, Bartosch L, & Garst M (2012) Mott metal-insulator transition on compressible lattices. *Phys Rev Lett* 109(17):176401.
38. Kadanoff LP, *et al.* (1967) Static phenomena near critical points: Theory and experiment. *Rev Mod Phys* 39(2):395-431.
39. Kotliar G, Lange E, & Rozenberg MJ (2000) Landau Theory of the Finite Temperature Mott Transition. *Phys Rev Lett* 84(22):5180-5183.
40. Postorino P, *et al.* (2003) Pressure tuning of electron-phonon coupling: The insulator to metal transition in manganites. *Phys Rev Lett* 91(17):175501.
41. Congeduti A, *et al.* (2001) Infrared study of charge delocalization induced by pressure in the $La_{0.75}Ca_{0.25}MnO_3$ manganite. *Phys Rev B* 63(18):184410.
42. Rueff J-P & Shukla A (2010) Inelastic x-ray scattering by electronic excitations under high pressure. *Rev Mod Phys* 82(1):847-896.
43. Peng G, *et al.* (1994) High-resolution manganese x-ray fluorescence spectroscopy. Oxidation-state and spin-state sensitivity. *J Am Chem Soc* 116(7):2914-2920.
44. Eskes H, Tjeng LH, & Sawatzky GA (1990) Cluster-model calculation of the electronic structure of CuO: A model material for the high-Tc superconductors. *Phys Rev B* 41(1):288-299.
45. Fujimori A & Minami F (1984) Valence-band photoemission and optical absorption in nickel compounds. *Phys Rev B* 30(2):957-971.
46. Ramesh R & Spaldin NA (2007) Multiferroics: progress and prospects in thin films. *Nature Mater* 6(1):21-29.
47. Bocquet AE, *et al.* (1996) Electronic structure of early 3d-transition-metal oxides by analysis of the 2p core-level photoemission spectra. *Phys Rev B* 53(3):1161-1170.
48. Herwadkar A & Lambrecht WRL (2009) Electronic structure of CrN: A borderline Mott insulator. *Phys Rev B* 79(3):035125.
49. Goodenough JB, Longo JM, & Kafalas JA (1968) Band antiferromagnetism and the new perovskite $CaCrO_3$. *Mater Res Bull* 3(6):471-481.
50. Qian J, *et al.* (2012) Polycrystalline diamond cutters sintered with magnesium carbonate in cubic anvil press. *Int J Refract Met Hard Mater* 31(0):71-75.
51. Wang S, He D, Wang W, & Lei L (2009) Pressure calibration for the cubic press by differential thermal analysis and the high-pressure fusion curve of aluminum. *High Pressure Res* 29(4):806-814.
52. Shen G & Wang Y (2014) High-pressure Apparatus Integrated with Synchrotron Radiation. *Spectroscopic Methods in Mineralology and Materials Sciences,* Reviews in Mineralogy & Geochemistry, eds Henderson GS, Neuville DR, & Downs RT), Vol 78, pp 745-777.
53. Kresse G & Joubert D (1999) From ultrasoft pseudopotentials to the projector augmented-wave method. *Phys Rev B* 59(3):1758-1775.